

## **Modulation of Crystallization Kinetics Using a Guest Acceptor for High-Performance Organic Solar Cells**

### **Achieving 19.8% Efficiency**

Lin Xie, Zhenyu Chen, Daobin Yang,\* Xueliang Yu, Xinyu Tong, Jinfeng Ge, Wei Song, Shuncheng Yang, Jintao Zhu, Pengfei Ding, Guanghao Lu, Xuke Li, Ming Long, Jing Li, Bingsuo Zou, Tao Liu\*, Quan Liu,\* Ziyi Ge\*

## Experimental Procedures

### 1. Material and synthesis

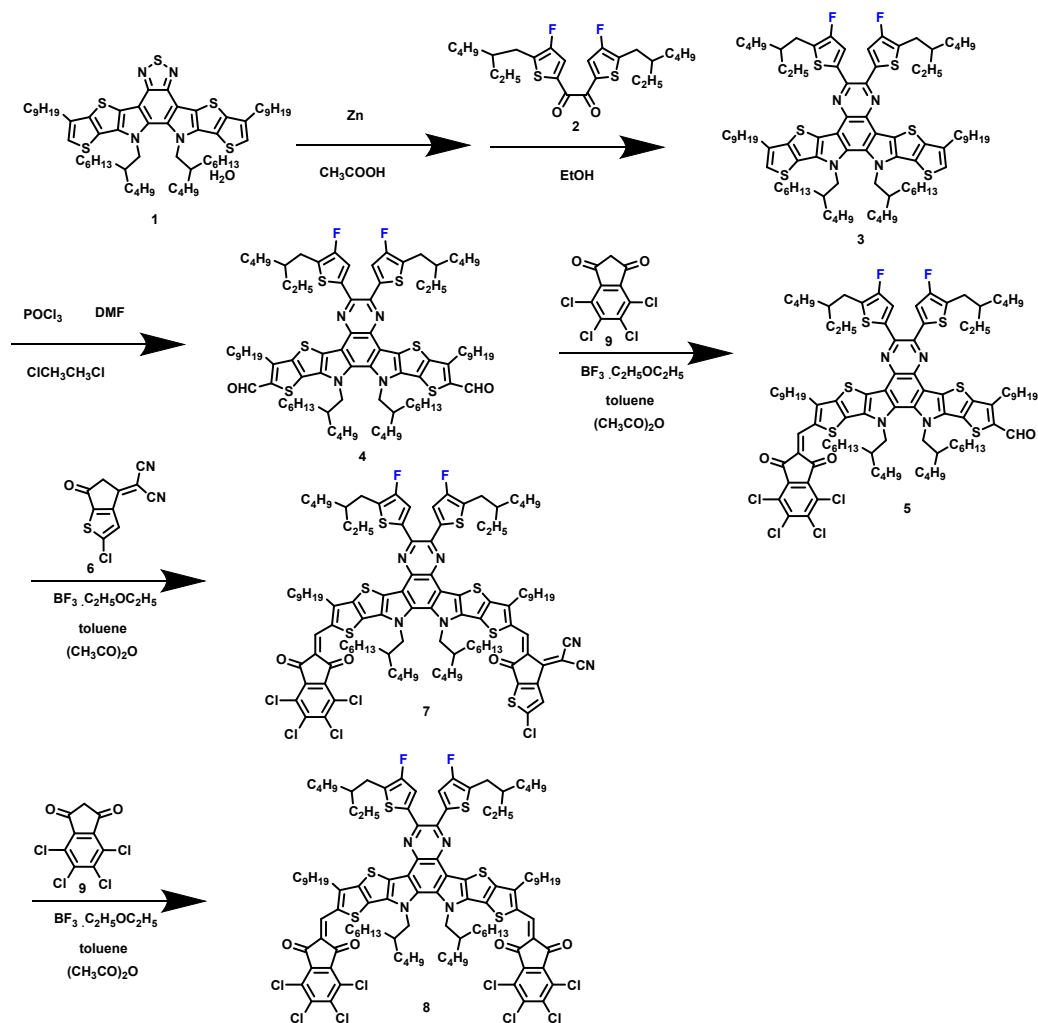
#### Design detail:

BTP-eC9, as Y derivatives featured with A-D-A'-D-A structure, became a star acceptor recently, ascribed to its extraordinary intermolecular interaction showing low bandgap, high electron mobility, rational phase separation when it is blended with PM6<sup>1, 2</sup>. Hence, PM6:BTP-eC9 was adopted as host system, and Y-series structure was chosen as guest component for further molecular modification. The rational design for the guest acceptor is to reduce the intramolecular charge transfer to acquire the wide bandgap material, which is conducive to the compensative absorption for host system and elevate the LUMO level to acquire higher optical bandgap. Therefore, this work adopted two strategies to design the novel guest acceptors: core engineering and terminal engineering. Herein, as shown in **Figure 1a**, two novel small molecular acceptors Qx-5Cl and Qx-8Cl were design and synthesized according to the following strategies: (i) core engineering: BTP-eC9 adopts benzothiadiazole unit (BDT) as the electron deficient core (A')<sup>3</sup>. Compared with the BDT moiety, the quinoidal-resonance quinoxaline (Qx) unit shows poorer electron affinity<sup>4</sup>, due to the presence of the imine nitrogen atoms, leading to blue-shifted absorption spectrum which can show complementary absorption for BTP-eC9. Moreover, the quinoxaline moiety enables more opportunities for the structural functionality of the acceptors<sup>5, 6</sup>. Hence, quinoxaline was chosen for the guest acceptor. (ii) Symmetric and asymmetric terminal engineering: 5,6-dichloro-3-(dicyanomethylene) indanone (IC-2Cl) was used for BTP-eC9 with symmetric terminal groups, processing strong electron-withdrawing ability resulting in strong intramolecular interaction and thus red-shifted absorption spectrum. Therefore, the compensational absorption spectrum is needed for the third component. In order to achieve blue-shifted absorption with elevated LUMO, 4,5,6,7-tetrachloroindane-1,3-dione (I-4Cl) was adopted to decrease the intramolecular interaction for Qx-8Cl as I-4Cl does not have cyano-group. Unlike symmetrical modification of the terminal group, asymmetric terminal groups with different electron-withdrawing ability to avoid a substantial adjustment of charge transport and aggregation behaviors of blend films. Hence, asymmetric molecule Qx-5Cl adopted a weak electron-withdrawing ability I-4Cl and a moderate electron-withdrawing ability T-Cl<sup>7</sup> (2-(1-chloro-6-oxo-5,6-dihydro-4H-cyclopenta[c]thiophen-4-ylidene) malononitrile) for each side of terminal groups. Briefly, the asymmetric end groups are adopted could subtly affect energy level and intramolecular interaction<sup>8</sup>.

#### Synthesis detail:

Super dry reagents were purchased from J&K and other conventional reagents were from SCRC. PM6 and PDINN were purchased from Solarmer Energy Inc. 2PACz was bought from the Tokyo Chemical Industry (TCI). 1,8-Diiodooctane was from TCI. The ITO glass was purchased from Suzhou Shangyang Solar Technology Co., Ltd. All reagents were directly used without any further treatment, and all the reactions were carried out under anitrogen atmosphere.

12,13-bis(2-butyloctyl)-3,9-dinonyl-12,13-dihydro-[1,2,5]thiadiazolo[3,4-e]thieno[2'',3'':4',5']thieno[2',3':4,5]pyrrolo[3,2-g]thieno[2',3':4,5]thieno[3,2-b]indole hydrate (**Compound 1**) and 1,2-bis(5-(2-ethylhexyl)-4-fluorothiophen-2-yl)ethane-1,2-dione (Compound 2) were from JiangSu GR-Chem Biotech Co., Ltd. 4,5,6,7-tetrachloroindane-1,3-dione (I-4Cl) and 2-(1-chloro-6-oxo-5,6-dihydro-4H-cyclopenta[c]thiophen-4-ylidene) malononitrile (T-Cl) were purchased from Derthon Co., Ltd. <sup>1</sup>H NMR spectra of Compound 3, 4,5,7,8 are shown in **Figure S11-20**.



**Scheme S1.** Synthetic route for Qx-5Cl and Qx-8Cl.

Synthesis of 13,14-bis(2-butyloctyl)-6,7-bis(5-(2-ethylhexyl)-4-fluorothiophen-2-yl)-3,10-dinonyl-4c,8a,13,14-tetrahydrothieno [2'',3''':4',5'] thieno [2',3':4,5] pyrrolo [3,2-f] thieno [2'',3''':4',5'] thieno [2',3':4,5] pyrrolo [2,3-h] quinoxaline (**compound 3**): Zinc powder (1.8916 mg, 29.10  $\mu\text{mol}$ ) was added into a solution of compound 1 (997.8 mg, 0.9709 mmol) in acetic acid (20 ml) in three-necked flask under nitrogen. Then the mixture was heated to 110°C for 30 min. After the mixture was cooled to room temperature, the solid was removed by filtration. The mixture solution was extracted with dichloromethane. Then the organic phase was removed under reduced pressure and a dark green solid was obtained. The solid and compound 2 (964 mg, 1.94 mmol) was added into a mixed solution of EtOH:CH<sub>3</sub>COOH=1:1 without further purification. Then the mixture was heated to 110°C for 1 h. After the mixture solution was cooled to room temperature, it was extracted with dichloromethane. The solvent was removed under reduced pressure. Then the organic phase was purified by silica gel column chromatography (PE:DCM=2:1 v/v) to obtain an orange solid 3 (399.5 mg, 29%). <sup>1</sup>H NMR (400 MHz, CD<sub>2</sub>Cl<sub>2</sub>)  $\delta$ : 7.19 (s, 2H, ArH), 7.05 (s, 2H, ArH), 4.69 (d,  $J=8.0$  Hz, 4H, NCH<sub>2</sub>), 2.84-2.79 (m, 8H, CH<sub>2</sub>), 2.16 (m, 2H, CH<sub>2</sub>), 2.03 (m, 2H, CH<sub>2</sub>), 1.78-1.72 (m, 2H, CH), 1.43-1.27 (m, 44H, CH<sub>2</sub>, CH), 1.02-0.85 (m, 48H, CH<sub>3</sub>, CH<sub>2</sub>), 0.69-0.60 (m, 12H, CH<sub>3</sub>).

Synthesis of 13,14-bis(2-butyloctyl)-6,7-bis(5-(2-ethylhexyl)-4-fluorothiophen-2-yl)-3,10-dinonyl-13,14-dihydrothieno[2'',3''':4',5']thieno[2',3':4,5]pyrrolo[3,2-f]thieno[2'',3''':4',5']thieno[2',3':4,5]pyrrolo[2,3-h]quinoxaline-2,11-dicarbaldehyde (**Compound 4**): Compound 3 (399.5 mg, 0.28 mmol), 1,2-Dichloroethane (20 ml), DMF (0.5 ml) were mixed in three-necked flask under nitrogen. POCl<sub>3</sub> (0.5 ml) was added dropwise slowly. After reacting at 80°C overnight, the mixture was transferred to a funnel. Then added into saturated Na<sub>2</sub>CO<sub>3</sub> solution slowly, and kept stirring. After no bubble, the mixture was extracted with dichloromethane. The organic phase was purified by silica gel column chromatography (PE:DCM=1:2 v/v) to obtain a yellow solid 4 (388.0 mg, 92%). <sup>1</sup>H NMR (400 MHz, CDCl<sub>3</sub>)  $\delta$ : 10.15 (s, 2H, ArH), 7.26 (s, 2H, ArH), 4.67 (d,  $J=8.0$  Hz, 4H, NCH<sub>2</sub>), 3.24 (t,  $J=7.6$

Hz, 4H, CH<sub>2</sub>), 2.85-2.83 (d, *J*=6.8 Hz, 4H, CH<sub>2</sub>), 2.09 (m, 2H, CH<sub>2</sub>), 1.98-1.91 (m, 4H, CH<sub>2</sub>), 1.78-1.71 (m, 2H, CH), 1.51-0.85 (m, 90H, CH<sub>2</sub>, CH), 0.68-0.62 (m, 12H, CH<sub>3</sub>).

Synthesis of 13,14-bis(2-butyloctyl)-6,7-bis(5-(2-ethylhexyl)-4-fluorothiophen-2-yl)-3,10-dinonyl-11-((4,5,6,7-tetrachloro-1,3-dioxo-1,3-dihydro-2H-inden-2-ylidene)methyl)-13,14

dihydrothieno[2'',3'':4',5']thieno[2',3':4,5]pyrrolo[3,2-f]thieno[2'',3'':4',5']thieno[2',3':4,5]pyrrolo[2,3-h]quinoxaline-2-carbaldehyde (**Compound 5**): The statistical reaction referred to this work<sup>9</sup>. The compound 4 (600 mg, 0.3785 mmol) and 9 (1 equiv of the compound 4) were dissolved in toluene (50 ml). BF<sub>3</sub> · OEt<sub>2</sub> (0.3 ml) and acetic anhydride (0.5 ml) were added. After reacting at 25°C 2h, the solvent was removed under reduced pressure. Then the organic phase was purified by silica gel column chromatography (PE:DCM=2:1 v/v) to obtain a dark solid 5 (320 mg, 53%). The R<sub>f</sub> of desired product of TLC after 30 min reaction when the compound 9 had been used up has been included in the **Figure S21**. <sup>1</sup>H NMR (400 MHz, CDCl<sub>3</sub>) δ: 10.17 (s, 1H, ArH), 8.24 (s, 1H, ArH), 7.29 (s, 1H, ArH), 7.27 (s, 1H, ArH), 4.78-4.69 (m, 4H, NCH<sub>2</sub>), 3.25 (t, *J*=7.6 Hz, 4H, CH<sub>2</sub>), 2.86 (d, *J*=6.8 Hz, 4H, CH<sub>2</sub>), 2.20-2.14 (m, 2H, CH<sub>2</sub>), 1.99-1.86 (m, 4H, CH<sub>2</sub>), 1.77-1.74 (m, 2H, CH), 1.49-0.83 (m, 90H, CH<sub>2</sub>, CH), 0.72-0.62 (m, 12H, CH<sub>3</sub>).

Synthesis of (Z)-2-(5-((13,14-bis(2-butyloctyl)-6,7-bis(5-(2-ethylhexyl)-4-fluorothiophen-2-yl)-3,10-dinonyl-11-((4,5,6,7-tetrachloro-1,3-dioxo-1,3-dihydro-2H-inden-2-ylidene)methyl)-13,14-

dihydrothieno[2'',3'':4',5']thieno[2',3':4,5]pyrrolo[3,2-f]thieno[2'',3'':4',5']thieno[2',3':4,5]pyrrolo[2,3-h]quinoxaline-2-yl)methylene)-2-chloro-6-oxo-5,6-dihydro-4H-cyclopenta[b]thiophen-4-ylidene)malononitrile (**Compound 7**): Compound 5 (150mg, 0.076 mmol), (CH<sub>3</sub>CO)<sub>2</sub>O (0.5 ml), toluene (20ml), BF<sub>3</sub>·C<sub>2</sub>H<sub>5</sub>OC<sub>2</sub>H<sub>5</sub> (0.5 ml), and T-Cl (95mg, 0.405 mmol) were mixed in three-necked flask in the air. After reacting at 25°C 2h, the solvent was removed under reduced pressure. Then the organic phase was purified by silica gel column chromatography (PE:DCM=2:1 v/v) to obtain a dark solid 7 (130mg, 86%). <sup>1</sup>H NMR (400 MHz, CDCl<sub>3</sub>) δ: 8.87 (s, 1H, ArH), 8.18 (s, 1H, ArH), 7.81 (s, 1H, ArH), 7.30 (d, 1H, ArH), 4.80 (m, 4H, NCH<sub>2</sub>), 3.27 (dd, *J*=7.6 Hz, 4H, CH<sub>2</sub>), 2.87 (d, *J*=6.4 Hz, 4H, CH<sub>2</sub>), 2.30-2.24 (m, 2H, CH<sub>2</sub>), 1.94-1.83 (m, 4H, CH<sub>2</sub>), 1.78-1.74 (m, 2H, CH), 1.40-0.83 (m, 90H, CH<sub>2</sub>, CH), 0.74-0.64 (m, 12H, CH<sub>3</sub>). <sup>13</sup>C NMR (151 MHz, CDCl<sub>3</sub>) δ: 185.2, 184.9, 180.6, 156.7, 155.2, 153.5, 152.5, 150.4, 146.2, 146.0, 145.2, 145.1, 142.7, 140.1, 139.9, 138.5, 138.3, 136.5, 136.5, 136.4, 136.3, 136.0, 135.0, 134.8, 133.8, 133.7, 133.6, 133.3, 133.0, 132.8, 129.7, 129.1, 129.1, 125.7, 125.6, 122.9, 121.3, 119.4, 119.1, 118.9, 118.6, 118.4, 114.4, 69.0, 66.7, 55.8, 55.7, 41.0, 39.3, 39.3, 32.8, 32.0, 31.8, 31.7, 31.4, 31.2, 30.6, 30.5, 29.9, 29.8, 29.7, 29.6, 29.5, 29.4, 29.1, 28.2, 28.1, 28.0, 26.0, 25.7, 25.6, 25.5, 23.2, 23.1, 23.0, 22.8, 22.7, 22.6, 14.3, 14.2, 14.1, 14.0, 13.9, 13.9, 11.1. <sup>19</sup>F NMR (377 MHz, CDCl<sub>3</sub>) δ: -130.73, -130.78. HR-TOF-MS (APCI) *m/z*: [M+H]<sup>+</sup> calcd. for C<sub>107</sub>H<sub>127</sub>Cl<sub>5</sub>F<sub>2</sub>N<sub>6</sub>O<sub>3</sub>S<sub>7</sub>, 1984.9; found, 1984.7.

Synthesis of 2,2'-((13,14-bis(2-butyloctyl)-6,7-bis(5-(2-ethylhexyl)-4-fluorothiophen-2-yl)-3,10-dinonyl-13,14-

dihydrothieno[2'',3'':4',5']thieno[2',3':4,5]pyrrolo[3,2-f]thieno[2'',3'':4',5']thieno[2',3':4,5]pyrrolo[2,3-h]quinoxaline-2,11-diyl)bis(methanylylidene))bis(4,5,6,7-tetrachloro-1H-indene-1,3(2H)-dione) <sup>1</sup>H NMR (400 MHz, CDCl<sub>3</sub>) (**Compound 8**): Compound 5 (150mg, 0.076 mmol), (CH<sub>3</sub>CO)<sub>2</sub>O (0.5 ml), toluene (20ml), BF<sub>3</sub>·C<sub>2</sub>H<sub>5</sub>OC<sub>2</sub>H<sub>5</sub> (0.5 ml), and I-4Cl (95mg, 0.334 mmol) were mixed in three-necked flask in the air. After reacting at 25°C 2h, the solvent was removed under reduced pressure. Then the organic phase was purified by silica gel column chromatography (PE:DCM=2:1 v/v) to obtain a dark solid 7 (150mg, 97.4%). <sup>1</sup>H NMR (400 MHz, CDCl<sub>3</sub>) δ: 8.25 (s, 2H, ArH), 7.30 (s, 2H, ArH), 4.82 (m, 4H, NCH<sub>2</sub>), 3.26 (t, *J*=7.6 Hz, 4H, CH<sub>2</sub>), 2.87 (d, *J*=6.8 Hz, 4H, CH<sub>2</sub>), 2.25 (m, 2H, CH<sub>2</sub>), 1.93-1.89 (m, 4H, CH<sub>2</sub>), 1.78-1.75 (m, 2H, CH), 1.40-0.83 (m, 90H, CH<sub>2</sub>, CH), 0.74-0.64 (m, 12H, CH<sub>3</sub>). <sup>13</sup>C NMR (151 MHz, CDCl<sub>3</sub>) δ: 185.3, 184.9, 155.2, 153.5, 152.5, 146.3, 142.7, 140.1, 139.9, 138.4, 136.5, 136.4, 136.3, 136.1, 135.0, 134.9, 133.8, 133.3, 132.9, 129.7, 129.2, 129.1, 125.7, 125.6, 119.5, 119.0, 118.6, 118.4, 55.8, 41.0, 39.3, 32.8, 32.0, 31.7, 31.2, 30.6, 30.5, 30.0, 29.9, 29.7, 29.6, 29.5, 29.1, 28.1, 28.0, 26.0, 25.6, 25.5, 23.2, 23.1, 22.8, 22.7, 14.3, 14.2, 14.1, 14.0, 11.1. <sup>19</sup>F NMR (377 MHz, CDCl<sub>3</sub>) δ: -130.73. HR-TOF-MS (APCI) *m/z*: [M+H]<sup>+</sup> calcd. for C<sub>106</sub>H<sub>126</sub>Cl<sub>8</sub>F<sub>2</sub>N<sub>4</sub>O<sub>4</sub>S<sub>6</sub>, 2034.2; found, 2034.5.

## 2. Device fabrication

Small-area devices: The ITO substrates were purchased from szsunnytech Inc. The anti-flection coating was not applied in this work. Devices were fabricated with the conventional device structure of glass/ITO/2PACz/Active layer/PDINN/Ag. ITO-coated glass substrates were cleaned with detergent and ultrasonicated in deionized water, acetone and ethyl alcohol for 20 min each and subsequently blow-dried by nitrogen. The 2PACz (0.2 mg/ml in ethanol) was spin-cast onto the ITO surface at 3000 r.p.m. for 30 s and baked at 100 °C for 10 min in the air. For binary devices, the PM6:BTP-eC9 (1:1.2 weight ratio, the concentration of PM6 is 7.5 mg/ml with 0.5wt% 1,8-diiodooctane (DIO)) were dissolved in chloroform in a nitrogen-filled glove box and stirred overnight and heated at 40°C for 30min before fabrication. For ternary devices, PM6:BTP-eC9:Qx-5Cl and PM6:BTP-eC9:Qx-8Cl (1:1.05:0.15 weight ratio, the concentration of PM6 is 7.5 mg/ml with 0.5wt% 1,8-diiodooctane (DIO)) were dissolved in chloroform in a nitrogen-filled glove box and stirred overnight and heated at 40°C for 30min before fabrication. The blended solutions were spin-cast at 4000 rpm for 30 s followed by 10 mins thermal annealing. For the cathode interlayer, PDINN was dissolved in methanol at the concentration of 1 mg/ml and spin-coated onto the photoactive layer at 2000 r.p.m. for 1 min. Finally, a 150 nm Ag electrode were deposited on top of the active layers through a shadow mask under a vacuum about  $1 \times 10^{-5}$  Pa. The active area was 0.0484 cm<sup>2</sup>.

Mini-modules: The laser patterning of the organic solar minimodules, “P1”, “P2”, and “P3”, is conducted by means of a femtosecond laser from Wuhan Hero Optoelectronics ( $\lambda=1030$  nm) with 0.3 ps pulse width, in combination with a galvanometer scanner with f-theta lens and a focal length of 170 mm. The module manufacturing process details are described as follows: The glass/ITO substrates are “P1” laser-patterned, using a repetition rate of 0.5M Hz, power of 6.33W and speed of 2000mm/s. For the small-area devices, we used 2-PACz (SAM) as the HTL. However, for the mini-modules, which have a larger area of 25 cm<sup>2</sup>, SAM is less likely to perform well. Instead, we used a dilute solution of PEDOT:PSS (in a 1:1 volume ratio with deionized water) for the mini-modules. Then, the PEDOT:PSS solution is spin-coated on the cleaned P1-patterned ITO substrates (to illustrate the use of PEDOT:PSS as HTL in small-area device, the  $J-V$  curve and EQE curve of the Qx-5Cl based ternary device by with PEDOT:PSS as HTL are displayed in **Figure S24**). After thermal annealing at 150 °C in ambient air for 15 min, the substrates are transferred into N2-filled glovebox for the active layer and hole-blocking layer deposition, with fabricating parameters being the same as the small device, but using a larger solution volume of around 150  $\mu$ L for each mini-module sample. Subsequently, the “P2” laser patterning step is conducted using a repetition rate of 0.2M Hz, power of 1.67 W and speed of 4000mm/s. Finally, 100 nm Ag is thermally evaporated, followed by the “P3” laser patterning step with a repetition rate of 0.2M Hz, power of 6.67W and speed of 4000mm/s. 5cm $\times$ 5cm large-area modules were fabricated with active area of 17.3 cm<sup>2</sup> consisting of six series-connected subcells with a geometry fill factor (GFF) of 94.6%. The active area of each subcell is 2.728 cm<sup>2</sup> with a width of 6.2 mm and a length of 44 mm. In an optimal module,  $V_{OC}$  and  $J_{SC}$  should have negligible losses. The only significant loss is mainly from FF, which mostly rely on the width of the module. A  $J_{SC}$  of 4.21 mA/cm<sup>2</sup> was achieved by the mini-modules which is rational. Because  $4.2 \times 6 = 25.2$  mA/cm<sup>2</sup> is less than 27.9 mA/cm<sup>2</sup> (ternary device by with PEDOT:PSS as HTL). The photocurrent loss mainly originates from the film homogeneity, as different film thickness contributes to a certain variation in  $J_{SC}$ . The final  $J_{SC}$  of the mini-module is determined by the lowest photocurrent achieved in the subcells.

## 3. Device characterization and measurement

The  $J-V$  measurement was performed via the solar simulator (Newport-Oriel® Sol3A 450W). The intensity of the AM 1.5G spectra was calibrated by a certified standard silicon solar cell. The area of the tested solar cells was determined by an optical microscope. The effective areas of the cells were 0.0484 cm<sup>2</sup>. A solar cell QE tester (QE-R, Enli Technology Co., Ltd) calibrated with a 75W xenon lamp source standard probe was be utilized to obtain the external quantum efficiency (EQE) spectrums. In order to study the dependence of devices properties on light intensity, neutral density filters were used to tune the light intensity, which were calibrated by the standard Si solar cell. Spectrophotometer (Perkin-Elmer Lambda 950) was taken to test the UV-vis absorption spectrums. Electrochemical workstation (CHI660C) was performed to obtain the cyclic voltammetry. Surface morphology and phase diagram were performed by Veeco Dimension 3100V atomic force microscope. The atomic force microscopic (AFM) images were acquired using a Bruker Dimension EDGE in tapping mode. Grazing-incidence wide-angle X-ray scattering (GIWAXS) and the grazing-incidence small-angle X-ray scattering (GISAXS) analyses were conducted by Xeuss 3.0 UHR SAXS/WAXS equipment. EL and EQE EL measurements were performed by applying external voltage/current sources through the OSCs (REPS, Enlitech), which consists of a monochromator in combination with a Si-CCD detector. Highly sensitive EQE was measured using an integrated system (PECT-600, Enlitech), where the photocurrent was amplified and modulated by a lock-in instrument. Time-resolved femtosecond transient absorption (TA) spectroscopy were performed on an Ultrafast Helios pump-probe system in collaboration with a regenerative amplified laser system from Coherent.

## 4. Cyclic voltammetry

The energy levels for BTP-eC9, TB-S, TB-S1, and TB-S1-O were measured by cyclic voltammetry (CV), which were performed by using Ag/AgCl as reference electrode in anhydrous CH<sub>3</sub>CN solution, and ferrocene/ferrocenium (Fc/Fc<sup>+</sup>) as used as internal reference. The HOMO was calculated according to the following equations:

$$HOMO = - [E_{OX} + (4.8 - E_{FC})] eV$$

$$LUMO = E_g - HOMO$$

Where  $E_{OX}$  is the onset of oxidation and the  $E_g$  is the optical bandgap obtained from UV-vis spectra.

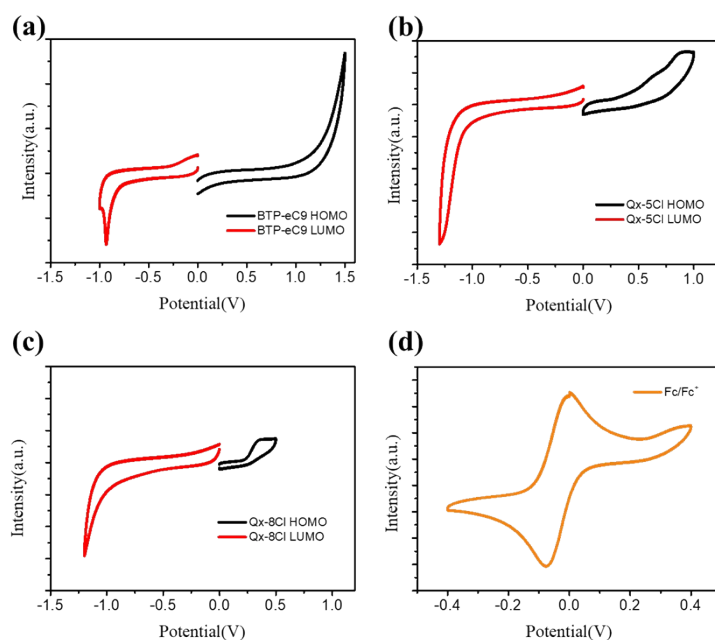


**Figure S1.** CV test for (a) Qx-5Cl, (b) BTP-eC9, and (d) Fc/Fc<sup>+</sup>.

## 5. In-situ Ultraviolet-visible (UV-vis) Absorption Measurements

In-situ UV-vis absorption measurements were performed by the Filmetrics F20-EXR spectrometer using the transmission mode with a time resolution of 0.05 s. The spectrometer consists of a light source and detector. The light source and detector are fixed above and below the substrate, respectively, and on the same vertical line. The solution was spined onto the substrate, and the film was formed on the glass substrate. The detector collects the transmission spectra ranging from 400 to 1050 nm during coating. The UV-vis absorption spectra are calculated from the transmission spectra according to the equation  $\Delta\lambda = -\log_{10}(T)$ , where  $\Delta\lambda$  is the absorbance at a certain wavelength ( $\lambda$ ), and T is the calculated transmittance. The light source and detector were turned on before coating the film, so time zero is the point when the first solution transmission spectrum was collected by the detector. Before time zero, there is only noise in the transmission spectra. The detailed instrument Schematic diagram can refer to this paper<sup>10</sup>.

## 6. In-situ Photoluminescence Spectra Measurements.

In-situ Photoluminescence Spectra Measurements were performed by a laser device (MGL-III-785-300mW BH81223) with a time resolution of 0.03 s. The excitation wavelength was 660 nm. For the process of in-situ measurement, during the film deposition process, the solution was spined onto the substrate, and the film was formed on the substrate. The light source emitted a beam of light, which was received by the detector after

passing through the sample. The absorption spectrum of the sample changed as the solvent evaporated. The spectrometer continuously recorded the absorption spectrum of the sample at different time points. By processing the recorded spectral data, the spectral changes of the sample during the film formation process can be obtained. By comparing the spectra at different time points, the spectral features and trends of the sample during the film formation process can be observed. By recording the time points of the absorption spectrum and comparing spectra at different time points, time-resolved observation of the formation process can be achieved, with the time resolution depending on the time interval of recording the spectrum and the speed of data processing. The detailed instrument Schematic diagram can refer to this paper<sup>10</sup>.

## 7. Film-depth-dependent characterization<sup>11</sup>.

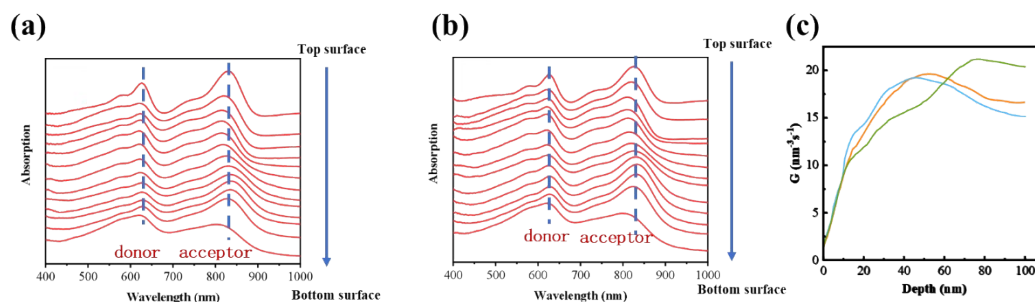


**Figure S2.** Film-depth-dependent absorption spectroscopy of (a) PM6:BTP-eC9, and (b) PM6:BTP-eC9:Qx-5Cl. (c) Dependence of the simulated exciton generation rate ( $G$ ) on the film depth for PM6:BTP-eC9, PM6:BTP-eC9:Qx-5Cl, and PM6:BTP-eC9:Qx-8Cl.

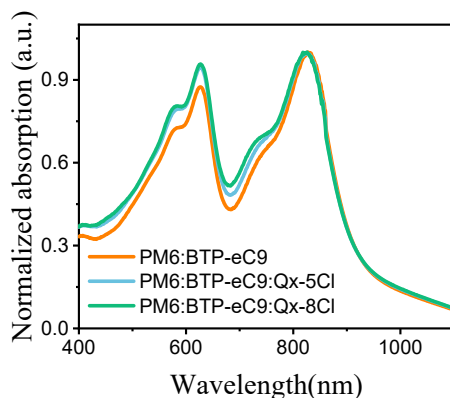


**Figure S3.** Absorption spectra of the blend films.

## 8. Photovoltaics properties

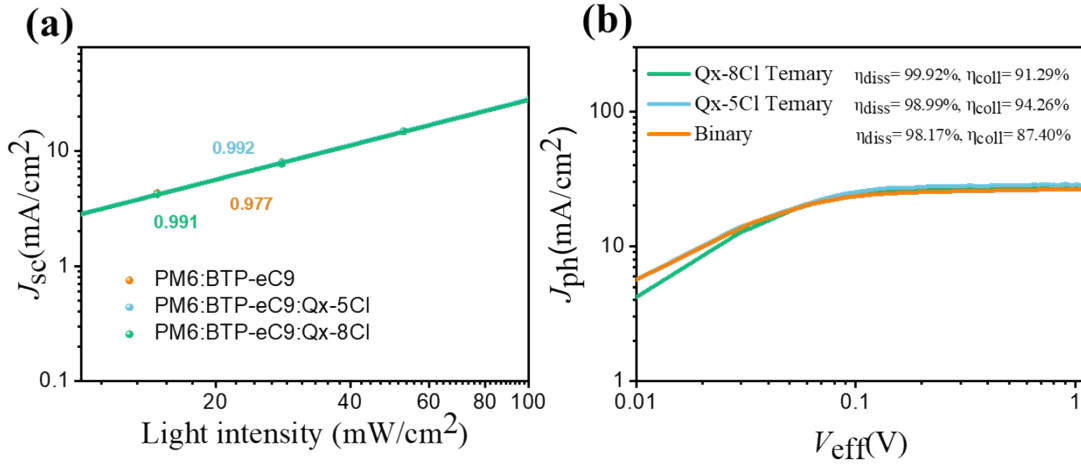


**Figure S4.** (a)  $J_{sc}$  depending on the variation of light intensity under a solar simulator. (b)  $J_{ph}$ - $V_{eff}$  curves of PM6:BTP-eC9, PM6:BTP-eC9:Qx-5Cl, and PM6:BTP-eC9:Qx-8Cl.

$J_{ph} = J_L J_D$ , where  $J_L$  is the current density in the condition of illumination while  $J_D$  is the value tested in the dark condition.  $V_{eff} = V_0 - V_{app}$ , where  $V_0$  equals the value when  $J_{ph}$  is 0, while  $V_{app}$  is defined as the applied external voltage. When the high  $V_{eff}$  is applied, the saturated photocurrent density  $J_{sat}$ , defined as all photogenerated excitons dissociating into free carriers is obtained.  $\eta_{diss} = J_{ph}$  (at the condition of short circuit) /  $J_{sat}$  and  $\eta_{coll} = J_{ph}$  (at the condition of maximum power output) /  $J_{sat}$ .  $\eta_{diss}$  describes the exciton dissociation ability and  $\eta_{coll}$  describes the free carrier collection ability. The  $\eta_{diss}/\eta_{coll}$  were calculated to be 98.17%/87.40%, 98.99%/94.26%, and 99.92%/91.29% for PM6:BTP-eC9, PM6:BTP-eC9:Qx-5Cl, and PM6:BTP-eC9:Qx-8Cl, respectively.

## 9. S-EQE and EL measurements.

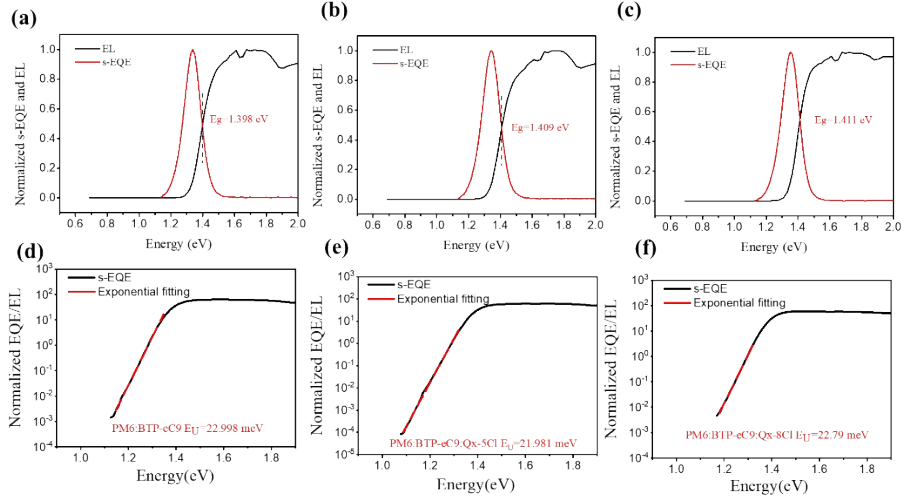


**Figure S5.** The normalized EL and the normalized s-EQE spectra of (a) PM6:BTP-eC9, (b) PM6:BTP-eC9:Qx-5Cl, and (c) PM6:BTP-eC9:Qx-8Cl. The Urbach energy fitting for PM6:BTP-eC9 (d), PM6:BTP-eC9:Qx-5Cl (e), and PM6:BTP-eC9:Qx-8Cl (f).

## 10. The calculation processes of $E_{loss}$

### 1. Radiative recombination above the bandgap ( $\Delta E_1$ )

$$\Delta E_1 = E_g - qV_{OC}^{SQ}$$

$$V_{OC}^{SQ} = \frac{KT}{q} \ln \left( \frac{J_{SC}}{J_0^{SQ}} + 1 \right) = \frac{KT}{q} \ln \left( \frac{q \int_0^{\infty} EQE_{PV}(E) \phi_{AM1.5}(E) dE}{q \int_{E_g}^{\infty} \phi_{BB}(E) dE} + 1 \right)$$

$$\phi_{BB}(E) = \frac{2\pi}{h^3 c^2} E^2 e^{-\frac{E}{KT}}$$

### 2. Radiative recombination below the bandgap ( $\Delta E_2$ )

$$\Delta E_2 = E_{loss,rad} = qV_{OC}^{SQ} - qV_{OC}^{rad}$$

$$V_{OC}^{rad} = \frac{KT}{q} \ln \left( \frac{J_{SC}}{J_0^{rad}} + 1 \right) = \frac{KT}{q} \ln \left( \frac{q \int_0^{\infty} EQE_{PV}(E) \phi_{AM1.5}(E) dE}{q \int_{E_0}^{\infty} \phi_{BB}(E) dE} + 1 \right)$$

### 3. Non-radiative recombination ( $\Delta E_3$ )

$$\Delta E_3 = E_{loss, non-rad} = -\frac{KT}{q} \ln \left( \frac{J_{SC}}{J_0^{rad}} + 1 \right)$$

where  $E_g$ ,  $V_{OC}^{SQ}$ ,  $K$ ,  $T$ ,  $q$ ,  $\phi_{BB}$ , and  $V_{OC}^{rad}$  are energy bandgap, Shockley-Queisser (SQ) open-circuit voltage limit, the Boltzmann constant, the temperature, the elementary charge, the black body spectrum and radiative recombination open-circuit voltage limit.

### 11. TA measurements.

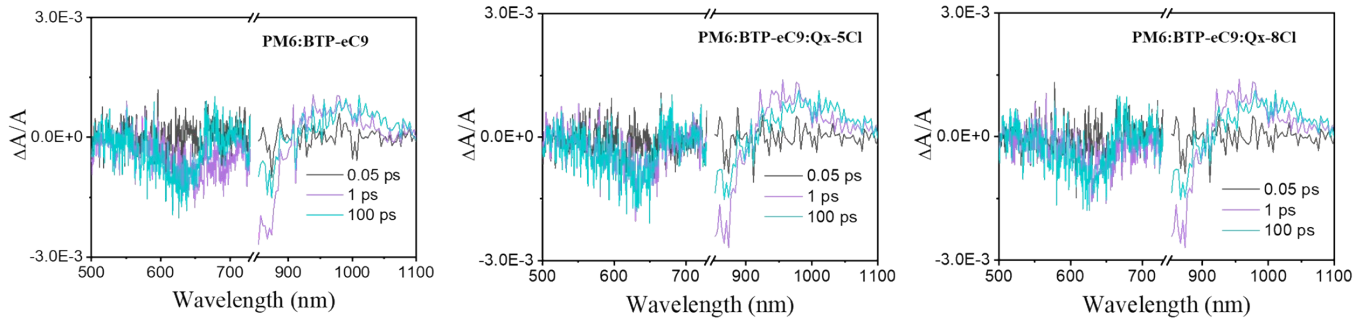


**Figure S6.** TA spectra in the range of 500-1100 nm of the blends at different delay times for PM6:BTP-eC9, PM6:BTP-eC9:Qx-5Cl, PM6:BTP-eC9:Qx-5Cl.

### 12. Contact angle measurement.

Contact angles were measured from spin-coated films by an optical contact angle meter (CAM 200). The surface energy was estimated by the Harmonic mean equations:

$$(1 + \cos\theta_1)\gamma_1 = 4 \left( \frac{\gamma_1^d \gamma_s^d}{\gamma_1^d + \gamma_s^d} + \frac{\gamma_1^p \gamma_s^p}{\gamma_1^p + \gamma_s^p} \right)$$

$$(1 + \cos\theta_2)\gamma_2 = 4 \left( \frac{\gamma_2^d \gamma_s^d}{\gamma_2^d + \gamma_s^d} + \frac{\gamma_2^p \gamma_s^p}{\gamma_2^p + \gamma_s^p} \right)$$

$$\gamma_s = \gamma_s^d + \gamma_s^p$$

where  $\gamma_s^d$  represents the dispersive components,  $\gamma_s^p$  is the polar component.  $\theta_1$  and  $\theta_2$  are the contact angles of pure water and diiodomethane, respectively. H<sub>2</sub>O:  $\gamma_1 = 72.8 \text{ mJ m}^{-2}$ ,  $\gamma_1^d = 21.8 \text{ mJ m}^{-2}$ ,  $\gamma_1^p = 51.0 \text{ mJ m}^{-2}$ ; diiodomethane:  $\gamma_2 = 50.8 \text{ mJ m}^{-2}$ ,  $\gamma_2^d = 48.5 \text{ mJ m}^{-2}$ ,  $\gamma_2^p = 2.3 \text{ mJ m}^{-2}$ .  $\gamma_s$  is the surface energy.

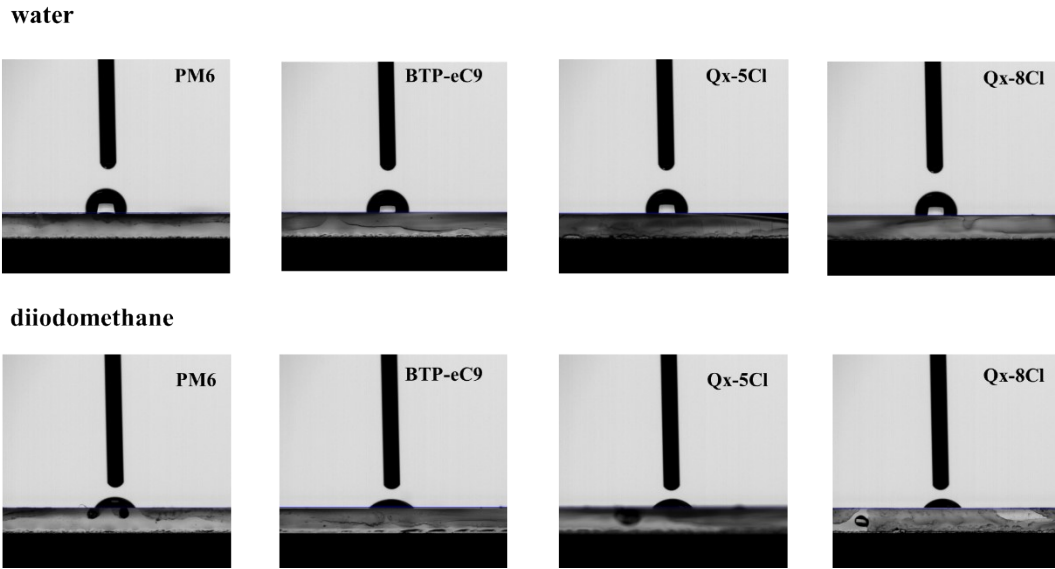


**Figure S7.** Contact angle images of PM6, BTP-eC9, Qx-5Cl and Qx-8Cl films with water and diiodomethane droplet on top.

**Table S1.** Summary of contact angles, surface tensions, and Flory-Huggins interaction parameters for PM6, BTP-eC9, and Qx-5Cl films

Surface	$\theta_{water} (^{\circ})$	$\theta_{diiodomethane} (^{\circ})$	$\gamma_s(\text{mN m}^{-1})$	$\chi^{D-A}$	$\chi^{A_1-A_2}$
PM6	101.06	65.03	25.74	/	/
BTP-eC9	92.86	52.22	33.03	0.454	/
Qx-5Cl	97.71	55.40	31.39	0.280	0.021
Qx-8Cl	97.34	57.65	29.99	0.162	0.073

### 13. Morphology characterization

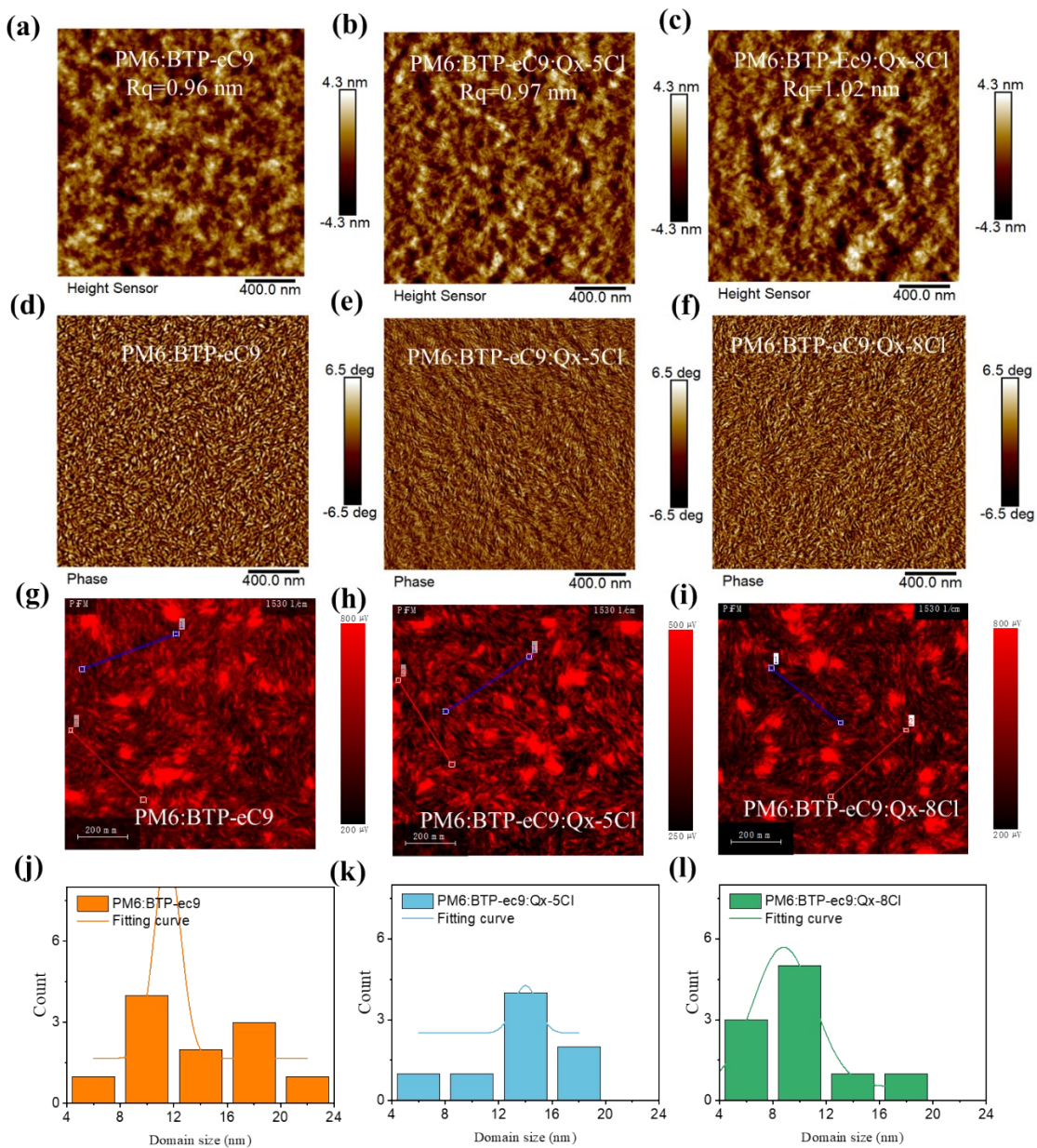


**Figure S8.** AFM height images for PM6:BTP-eC9 (a), PM6:BTP-eC9:Qx-5Cl (b) PM6:BTP-eC9:Qx-8Cl (c) ; and phase images for PM6:BTP-eC9 (d), PM6:BTP-eC9:Qx-5Cl (e), and PM6:BTP-eC9:Qx-8Cl (f); piFM images of PM6:BTP-eC9 (g), PM6:BTP-eC9:Qx-5Cl (h), and PM6:BTP-eC9:Qx-8Cl (i). (j-l) Statistical data extracted from Pi-FM measurements of PM6:BTP-eC9, PM6:BTP-eC9:Qx-5Cl, and PM6:BTP-eC9:Qx-8Cl.

**Table S2.** The diffraction vector ( $q$ ) values of diffraction peaks,  $\pi$ - $\pi$  distance, and FWHM crystal correlation lengths (CCLs) of neat films and the binary and ternary blend films along with out-of-plane direction.

	$q$ ( $\text{\AA}^{-1}$ )	$\pi$ - $\pi$ distance ( $\text{\AA}$ )	CCL ( $\text{\AA}$ )	FWHM
PM6 <sup>12</sup>	1.647	3.813	22.920	0.274
BTP-eC9	1.665	3.772	21.288	0.295
Qx-5Cl	1.652	3.801	21.361	0.294
Qx-8Cl	1.705	3.683	22.590	0.278
PM6: BTP-eC9	1.665	3.772	21.958	0.286
PM6: BTP-eC9:Qx-5Cl	1.665	3.772	22.509	0.279
PM6: BTP-eC9:Qx-8Cl	1.697	3.700	20.933	0.300

**Table S3.** The diffraction vector ( $q$ ) values of diffraction peaks,  $d$  spacing, and FWHM crystal correlation lengths (CCLs) of neat films and the binary and ternary blend films along with in-plane direction.

	$q$ ( $\text{\AA}^{-1}$ )	$d$ spacing ( $\text{\AA}$ )	CCL ( $\text{\AA}$ )	FWHM
PM6 <sup>12</sup>	0.288	21.806	60.971	0.103
BTP-eC9	0.369	17.019	66.105	0.095
Qx-5Cl	0.316	19.873	67.527	0.093
Qx-8Cl	0.393	15.980	50.645	0.124
PM6: BTP-eC9	0.287	21.881	64.742	0.097
PM6: BTP-eC9:Qx-5Cl	0.279	22.509	66.105	0.095
PM6: BTP-eC9:Qx-8Cl	0.295	21.288	89.714	0.070

**Table S4.** Morphology parameters fitted by the GISAXS profiles ( $\xi$  is the intermixing domain size;  $R_g$  is the crystal domain size)

Active layer	$\xi$ (nm)	$R_g$ (nm)
PM6: BTP-eC9	36	22.2
PM6: BTP-eC9:Qx-5Cl	40	24.2
PM6: BTP-eC9:Qx-8Cl	45	19.7

## 14. Photocatalytic degradation

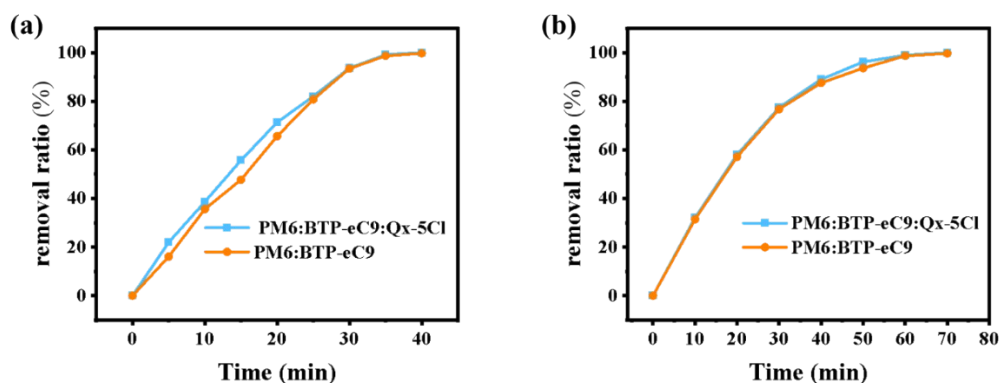


**Figure S9.** Photocatalytic degradation of carbamazepine using different photocatalysts under two sunlight irradiation intensities: (a) 300 W xeon light and (b) 50 W visible led lamp.

Moreover, many of the highest performing materials used for organic photocatalytic nanoparticles (NPs) had already displayed high OPV performance due to their similar working mechanism<sup>13-16</sup>. By monitoring the degradation of carbamazepine under xenon lamp irradiation, **Figure S8** shows the comparative performance of the prepared photocatalysts. The ternary PM6:BTP-eC9:Qx-5Cl composite with coconut shell charcoal as the substrate can achieve the complete removal of carbamazepine within 40 min of light exposure under 300 W xeon light, showing stronger photocatalytic activity compared to the binary PM6:BTP-eC9 composite. **Figure S8** shows that the degradation rate of carbamazepine solution with a mass concentration of 10 mg/L under 50 W visible light irradiation could reach more than 100% in 70 min of light irradiation, which demonstrated the better degradation effect of the photocatalyst PM6:BTP-eC9:Qx-5Cl under different light intensities. The material still exhibits excellent photocatalytic performance after 20 cycles, demonstrating its renewable and recyclable properties. These results indicate that Qx-5Cl included into the PM6: BTP-eC9 host system can be used in organic photocatalytic degradation application with improved performance.

**Table S5.** Device efficiencies for ternary devices by monitoring the solution phase to solid-state film transition of multi-acceptor-based bulk heterojunctions (BHJs) using *in situ* optical spectroscopy

Host system	Guest component	Binary performance (%)	Ternary performance (%)	Reference
PM6:BTP-eC9	Y6-1O	17.86	18.81	17
PM6:BTP-eC9	PC <sub>71</sub> BM	17.86	18.66	17
PM6:BTP-eC9	Y6-1O: PC <sub>71</sub> BM	17.86	19.35	17
PM6:BTP-eC9	BTR-Cl	16.83	17.5	10
PM6:BTP-eC9	PY-IT	17.53	19.41	18
PB2: BTP-eC9	FTCC-Br	17.8	19.5	19
PM6:N3	N2200	10.6 (blade-coated)	10.9 (blade-coated)	20

## 15. Stability under illumination

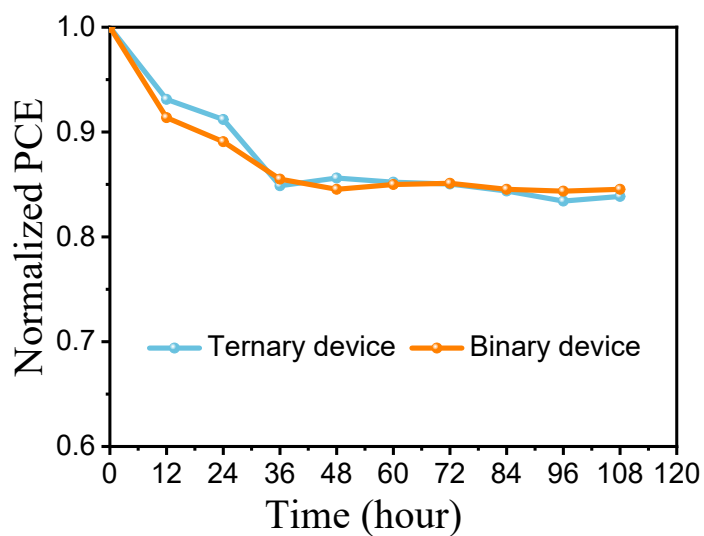


**Figure S10.** Normalized PCE of inverted devices of unencapsulated ternary device and binary device in the glovebox with illumination of 1-sun simulator ( $100 \text{ mW cm}^{-2}$ ).

## 16. $^1\text{H}$ NMR Spectra and TLC results

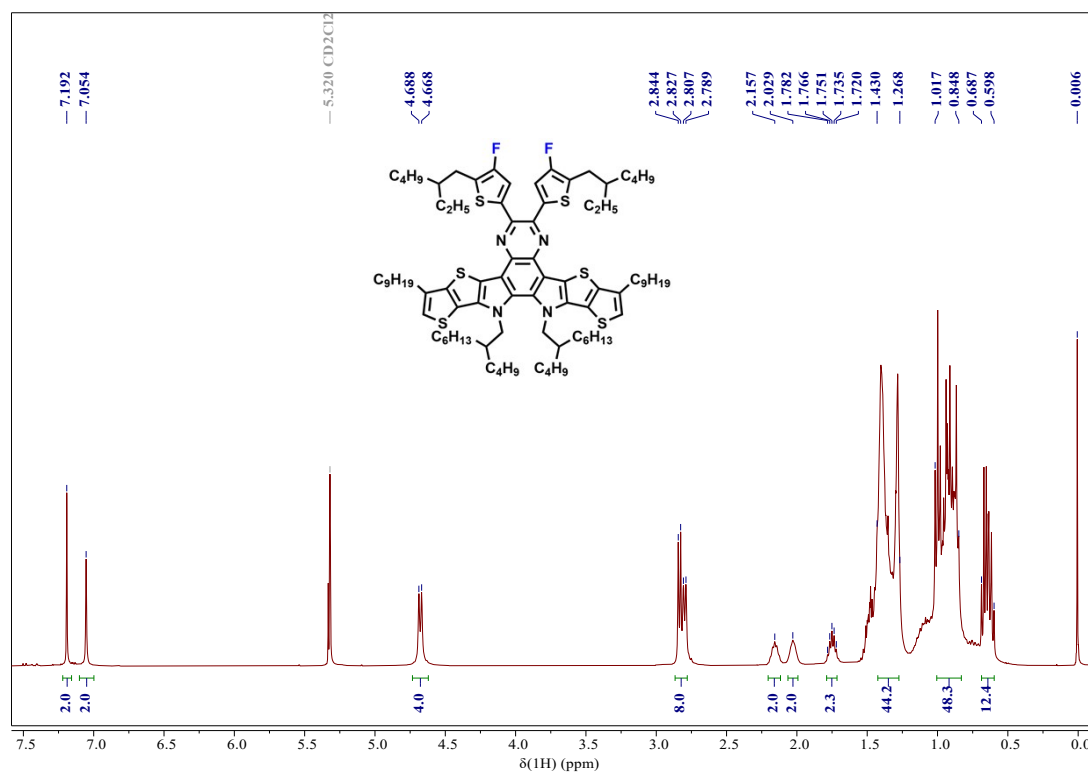


**Figure S11.**  $^1\text{H}$  NMR spectrum Compound 2.

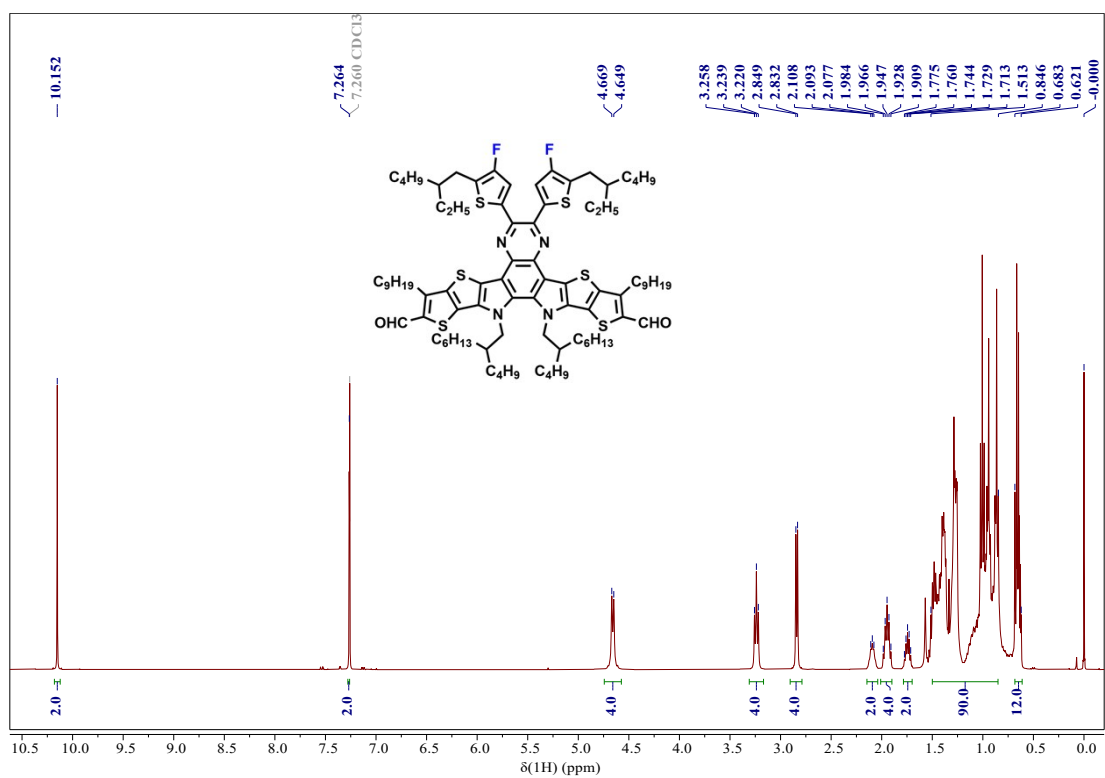


Figure S12. <sup>1</sup>H NMR spectrum Compound 3.

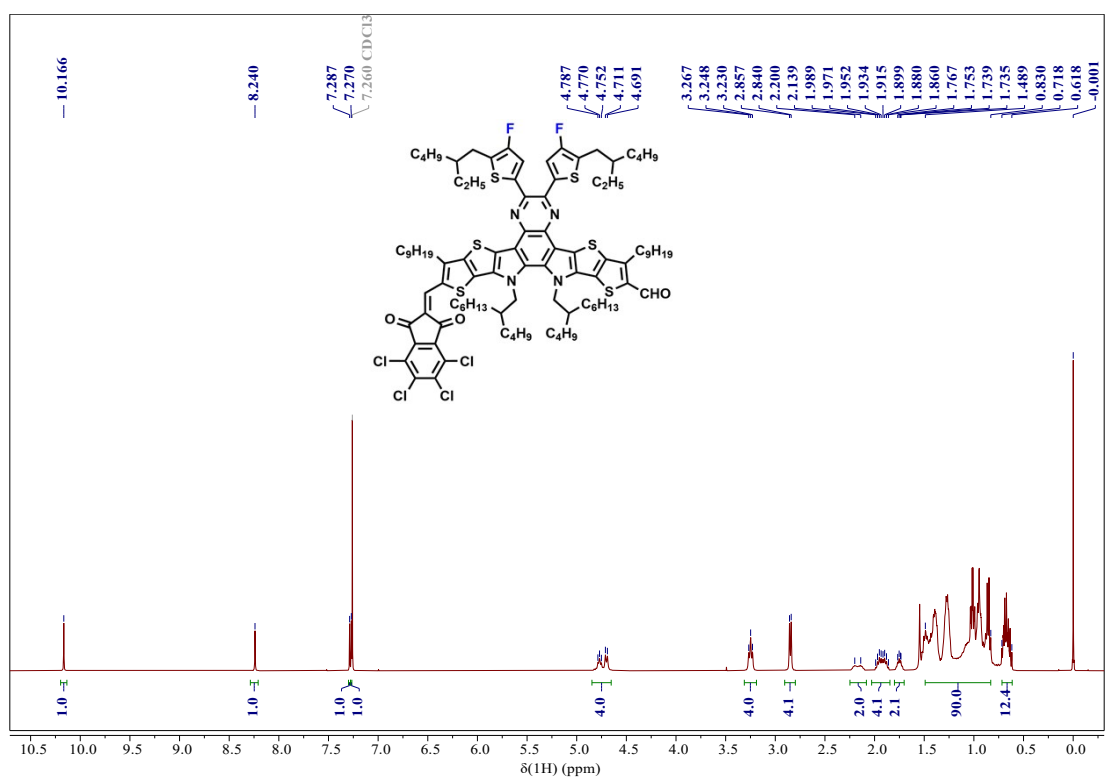


Figure S13. <sup>1</sup>H NMR spectrum Compound 5.

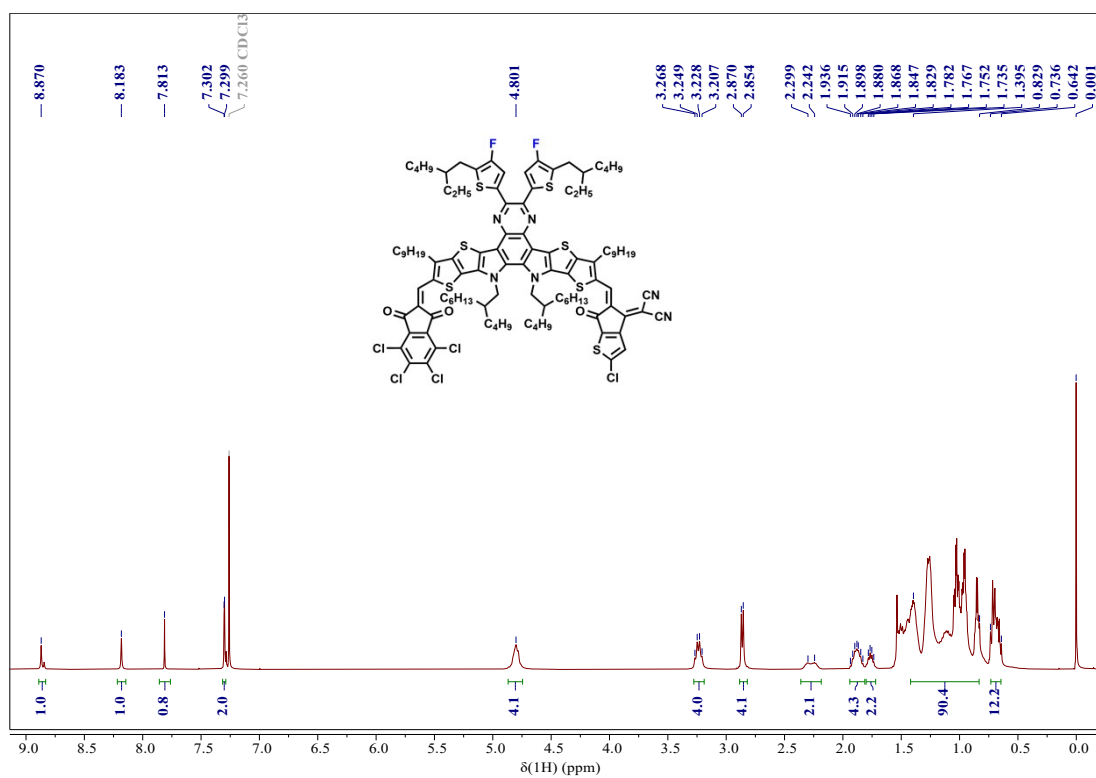


Figure S14. <sup>1</sup>H NMR spectrum Compound 7.

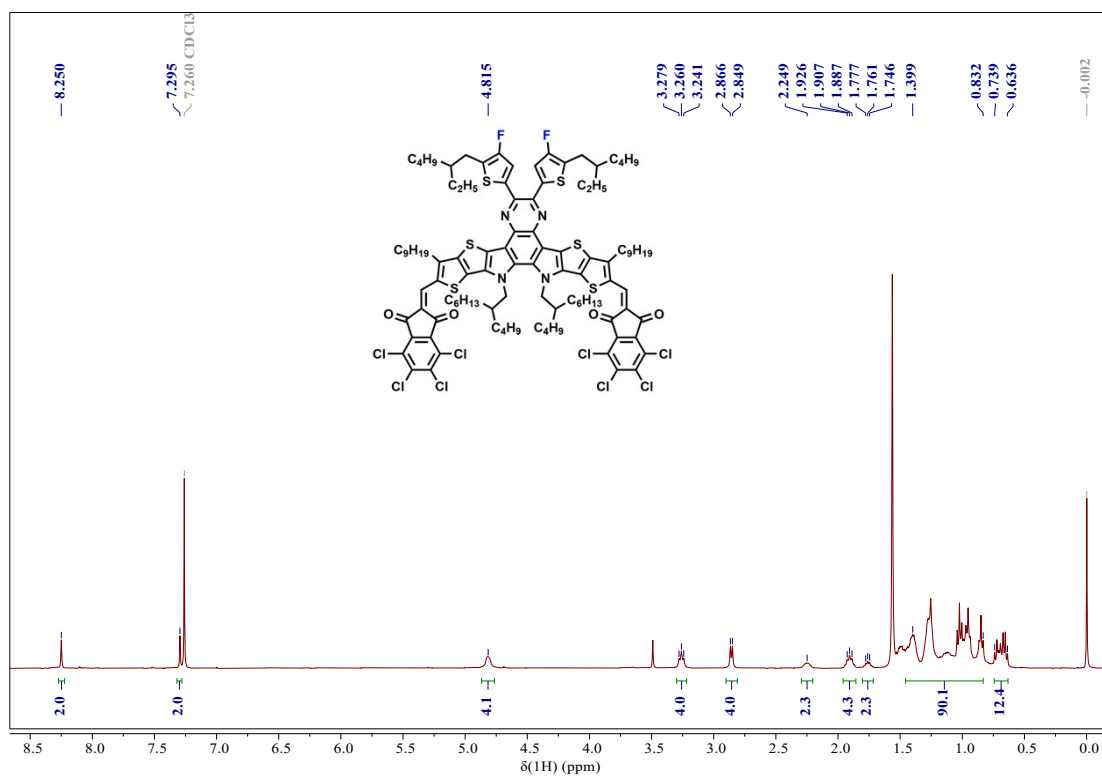
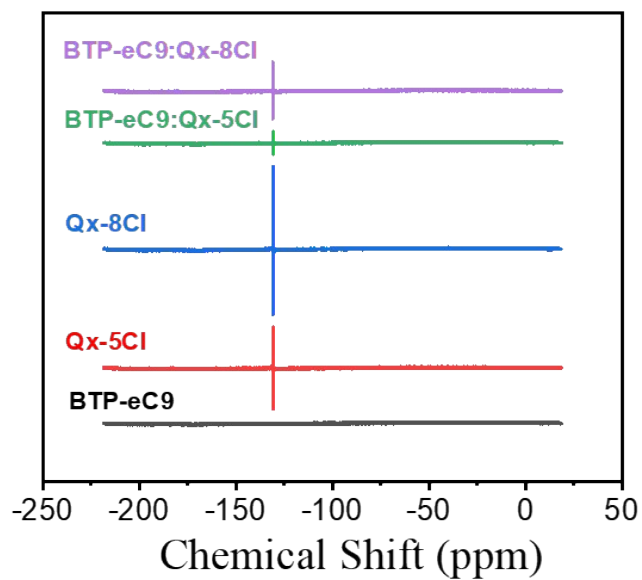
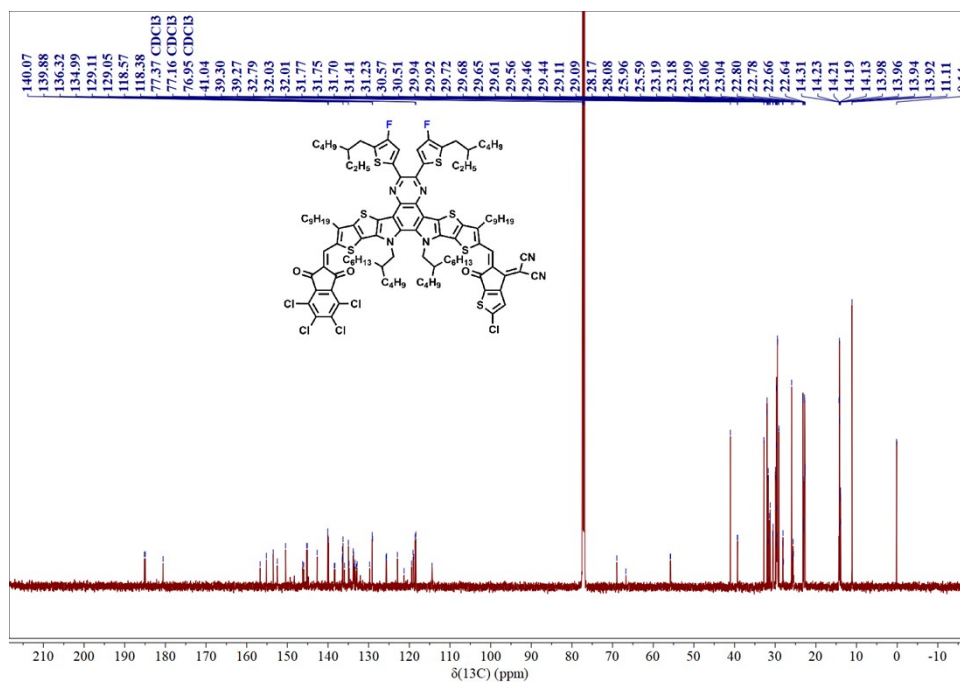


Figure S15. <sup>1</sup>H NMR spectrum Compound 8.



**Figure S16.**  $^{19}\text{F}$  NMR spectra of  $^{19}\text{F}$  HMR of BTP-eC9, Qx-5Cl, Qx-8Cl, the mixture of BTP-eC9:Qx-5Cl, and the mixture of BTP-eC9:Qx-8Cl.



**Figure S17.**  $^{13}\text{C}$  NMR spectrum Compound 7.

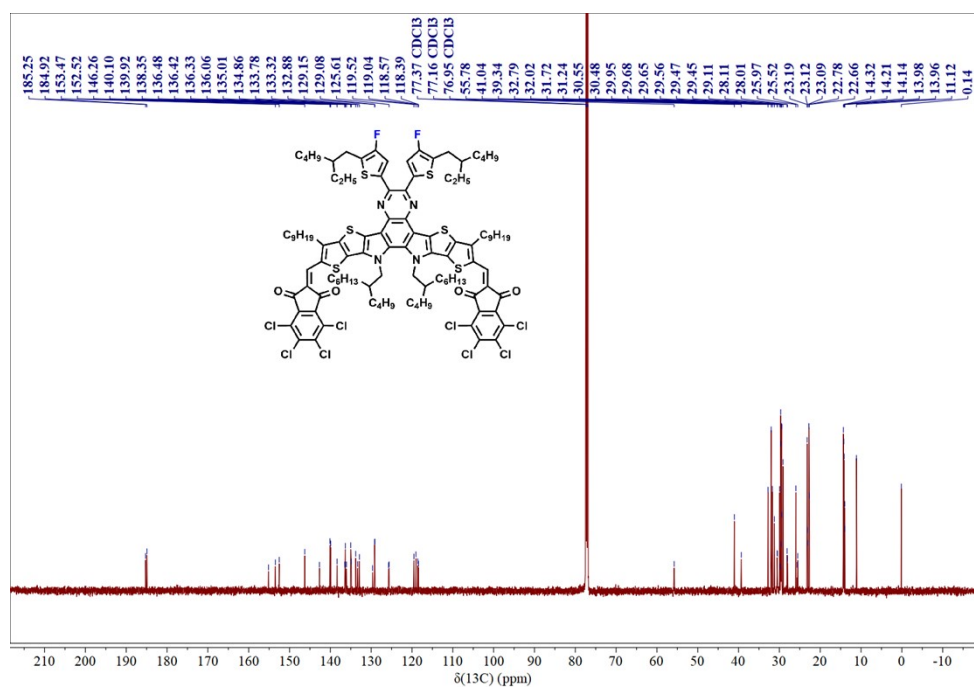


Figure S18.  $^{13}\text{C}$  NMR spectrum Compound 8.

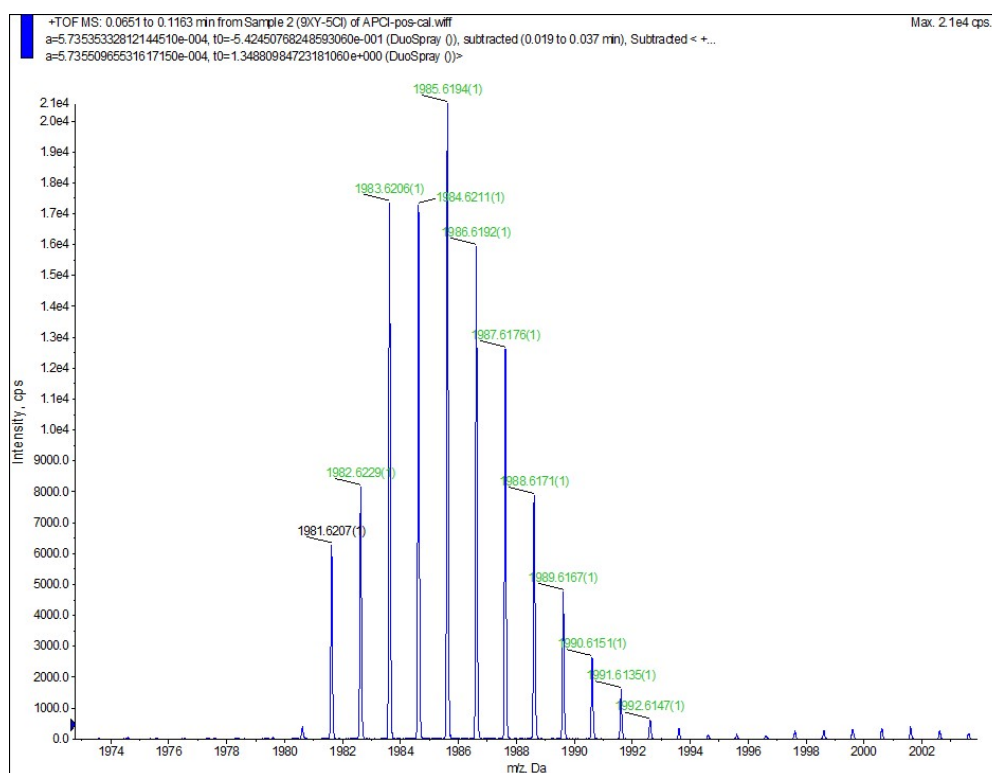


Figure S19. TOF-MS spectrum Compound 7.

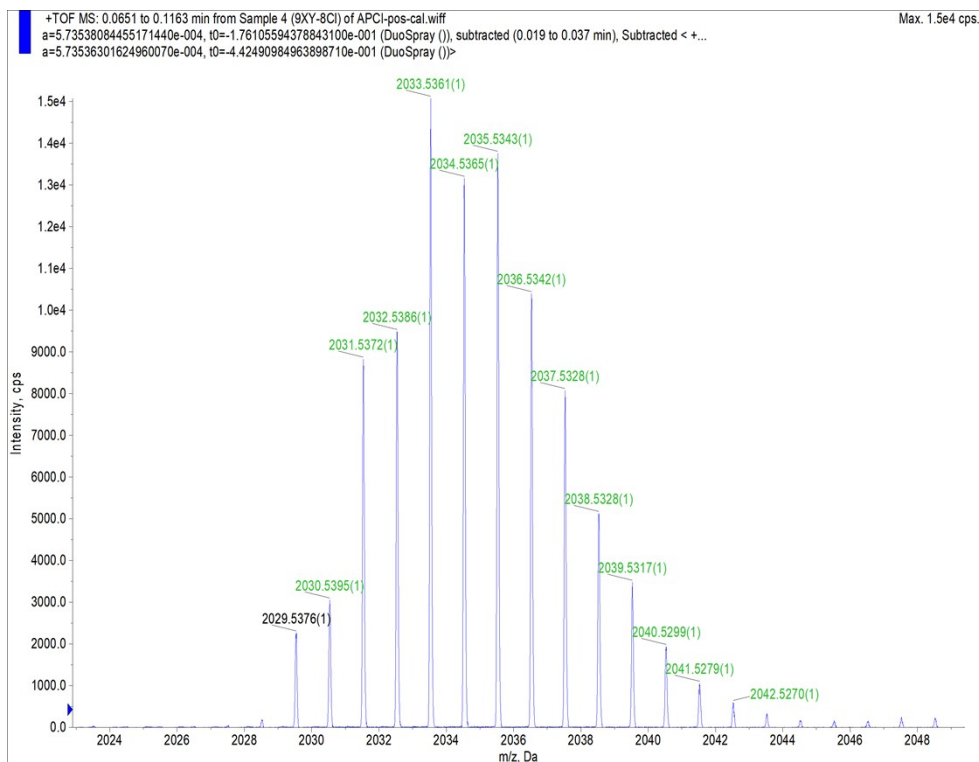


Figure S20. TOF-MS spectrum Compound 8.

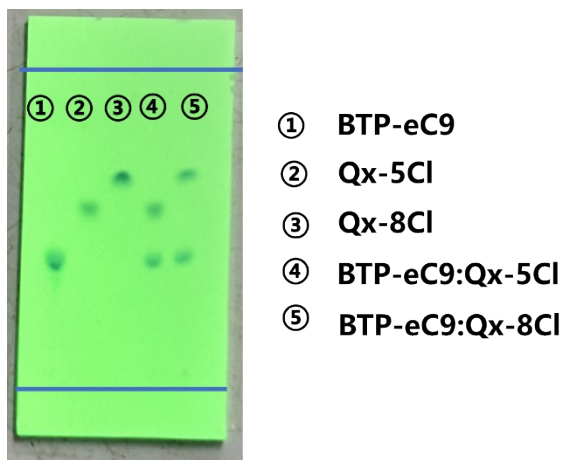
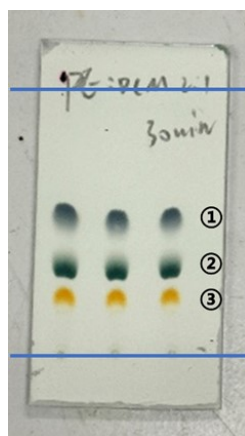


Figure S21. Thin-layer chromatography for different solutions.



disubstituted  
mono-sub  
Compound 4

Figure S22. The Rf of desired product of TLC after 30 min reaction during the synthesis of compound 5.

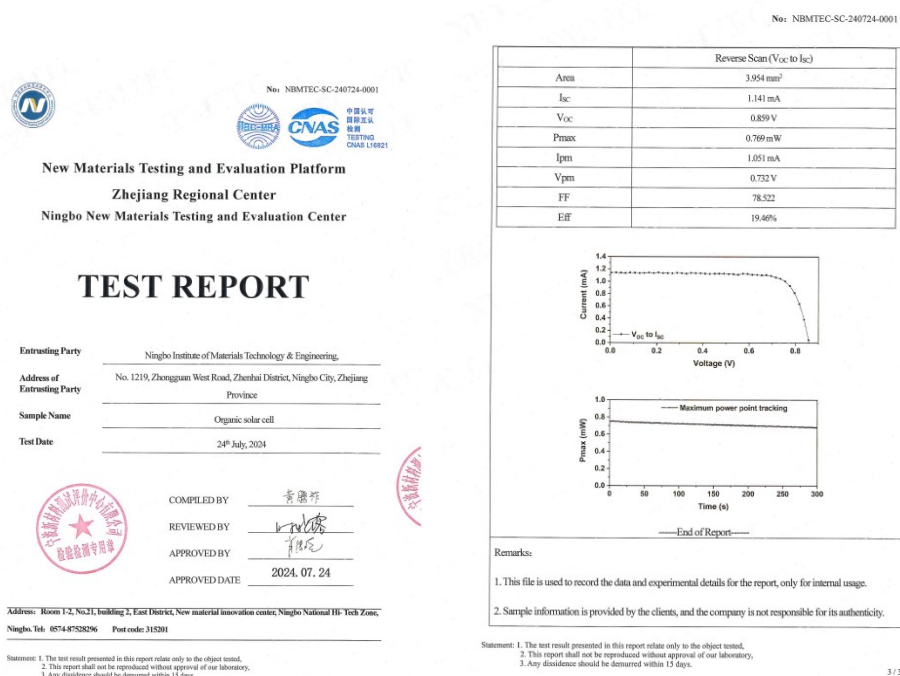


Figure S23. The certification report of the champion OPV device.

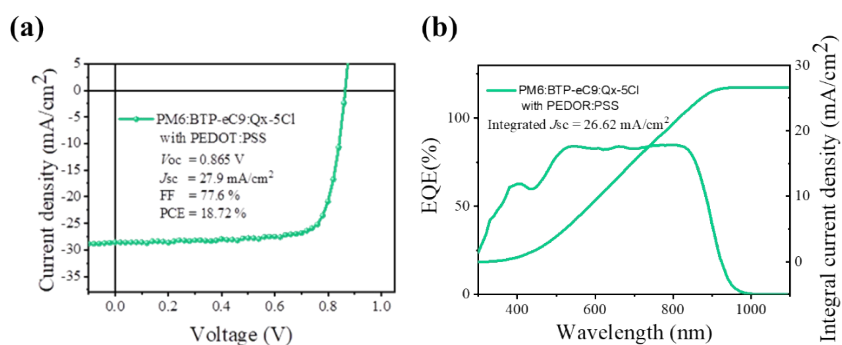


Figure S24. (a) The  $J$ - $V$  curve and (b) the EQE spectra of Qx-5Cl based ternary device by applying PEDOT:PSS as HTL.

## References

1. S. Li, C.-Z. Li, M. Shi and H. Chen, *ACS Energy Letters*, 2020, **5**, 1554-1567.
2. H. Yao and J. Hou, *Angew. Chem. Int. Ed.*, 2022, **61**, e202209021.
3. Q. Wei, W. Liu, M. Leclerc, J. Yuan, H. Chen and Y. Zou, *Sci. China Chem.*, 2020, **63**, 1352-1366.
4. Z. Chen, J. Ge, Y. Guo, M. Zhao, J. Shi, Y. Qiu, E. Zhou and Z. Ge, *ACS Energy Lett.*, 2022, **7**, 3432-3438.
5. K. Liu, Y. Jiang, G. Ran, F. Liu, W. Zhang and X. Zhu, *Joule*, DOI: 10.1016/j.joule.2024.01.005.
6. Z. Chen, J. Zhu, D. Yang, W. Song, J. Shi, J. Ge, Y. Guo, X. Tong, F. Chen and Z. Ge, *Energy Environ. Sci.*, 2023, **16**, 3119-3127.
7. Y. Cui, Y. Wang, J. Bergqvist, H. Yao, Y. Xu, B. Gao, C. Yang, S. Zhang, O. Inganäs, F. Gao and J. Hou, *Nat. Energy*, 2019, **4**, 768-775.
8. D. Li, C. Sun, T. Yan, J. Yuan and Y. Zou, *ACS Cent. Sci.*, 2021, **7**, 1787-1797.
9. H. Fu, J. Yao, M. Zhang, L. Xue, Q. Zhou, S. Li, M. Lei, L. Meng, Z.-G. Zhang and Y. Li, *Nature Communications*, 2022, **13**, 3687.
10. J. Xue, H. Zhao, C. Zhao, L. Tang, Y. Wang, J. Xin, Z. Bi, K. Zhou and W. Ma, *Advanced Functional Materials*, 2023, **33**, 2303403.
11. Z. Shen, Y. Jiang, J. Yu, Y. Zhu, L. Bu and G. Lu, *Adv. Energy Mater.*, 2021, **8**, 2101476.
12. L. Xie, A. Lan, Q. Gu, S. Yang, W. Song, J. Ge, R. Zhou, Z. Chen, J. Zhang, X. Zhang, D. Yang, B. Tang, T. Wu and Z. Ge, *ACS Energy Letters*, 2023, **8**, 361-371.
13. J. Kosco, M. Bidwell, H. Cha, T. Martin, C. T. Howells, M. Sachs, D. H. Anjum, S. Gonzalez Lopez, L. Zou, A. Wadsworth, W. Zhang, L. Zhang, J. Tellam, R. Sougrat, F. Laquai, D. M. DeLongchamp, J. R. Durrant and I. McCulloch, *Nature Materials*, 2020, **19**, 559-565.
14. J. Kosco, S. Gonzalez-Carrero, C. T. Howells, T. Fei, Y. Dong, R. Sougrat, G. T. Harrison, Y. Firdaus, R. Sheelamanthula, B. Purushothaman, F. Moruzzi, W. Xu, L. Zhao, A. Basu, S. De Wolf, T. D. Anthopoulos, J. R. Durrant and I. McCulloch, *Nature Energy*, 2022, **7**, 340-351.
15. A. Dolan, X. Pan, M. J. Griffith, A. Sharma, J. M. de la Perelle, D. Baran, G. F. Metha, D. M. Huang, T. W. Kee and M. R. Andersson, *Advanced Materials*, 2024, **n/a**, 2309672.
16. Z. Liu, Z. Jin, G. Li, X. Zhao and A. Badiei, *Energy Conversion and Management*, 2022, **251**, 114967.
17. W. Zhang, Y. Yue, R. Yang, Y. Zhang, W. Du, G. Lu, J. Zhang, H. Zhou, X. Zhang and Y. Zhang, *Energy & Environmental Science*, 2024, **17**, 2182-2192.
18. Y. Zhang, W. Deng, C. E. Petoukhoff, X. Xia, Y. Lang, H. Xia, H. Tang, H. T. Chandran, S. Mahadevan, K. Liu, P. W. K. Fong, Y. Luo, J. Wu, S.-W. Tsang, F. Laquai, H. Wu, X. Lu, Y. Yang and G. Li, *Joule*, 2023, **7**, 2873-2893.
19. J. Wang, P. Bi, Y. Wang, Z. Zheng, Z. Chen, J. Qiao, W. Wang, J. Li, C. An, S. Zhang, X. Hao and J. Hou, *CCS Chemistry*, 2023, **6**, 218-229.
20. Z. Peng, Y. Zhang, X. Sun, W. Zhao, F. Bian, Y. Geng, L. Ye and C. Yang, *Advanced Functional Materials*, 2023, **33**, 2213248.